The Cryosphere Discuss., 8, 4737–4778, 2014
www.the-cryosphere-discuss.net/8/4737/2014/
doi:10.5194/tcd-8-4737-2014

The Cryosphere Discussions
Open Access

Bimodal albedo distributions in the ablation zone of the southwestern Greenland Ice Sheet

S. E. Moustafa[1], A. K. Rennermalm[1], L. C. Smith[2], M. A. Miller[3], and J. R. Mioduszewski[1]

[1]Department of Geography, Rutgers, The State University of New Jersey, 54 Joyce Kilmer Avenue, Piscataway, NJ 08854-8045, USA
[2]Department of Geography, University of California, Los Angeles, 1255 Bunche Hall, P.O. Box 951524, Los Angeles, CA 90095-1524, USA
[3]Department of Environmental Sciences, Rutgers, The State University of New Jersey, 14 College Farm Rd, New Brunswick, NJ 08901-8551, USA

Received: 4 August 2014 – Accepted: 12 August 2014 – Published: 5 September 2014

Correspondence to: S. E. Moustafa (samiah.moustafa@rutgers.edu)

Published by Copernicus Publications on behalf of the European Geosciences Union.

Abstract

Surface albedo is a key variable controlling solar radiation absorbed at the Greenland Ice Sheet (GrIS) surface, and thus, meltwater production. Recent decline in surface albedo over the GrIS has been linked to enhanced snow grain metamorphic rates and amplified ice-albedo feedback from atmospheric warming. However, the importance of distinct surface types on ablation zone albedo and meltwater production is still relatively unknown, and excluded in surface mass balance models. In this study, we analyze albedo and ablation rates using in situ and remotely-sensed data. Observations include: (1) a new high-quality in situ spectral albedo dataset collected with an Analytical Spectral Devices (ASD) spectroradiometer measuring at 325–1075 nm, along a 1.25 km transect during three days in June 2013; (2) broadband albedo at two automatic weather stations; and (3) daily MODerate Resolution Imaging Spectroradiometer (MODIS) albedo (MOD10A1) between 31 May and 30 August. We find that seasonal ablation zone albedos have a bimodal distribution, with two alternate states. This suggests that an abrupt switch from high to low albedo can be triggered by a modest melt event, resulting in amplified surface ablation rates. Our results show that such a shift corresponds to an observed melt rate percent difference increase of 51.6 % during peak melt season (between 10–14 and 20–24 July 2013). Furthermore, our findings demonstrate that seasonal changes in GrIS ablation zone albedo are not exclusively a function of a darkening surface from ice crystal growth, but rather are controlled by changes in the fractional coverage of snow, bare ice, and impurity-rich surface types. As the climate continues to warm, regional climate models should consider the seasonal evolution of ice surface types in Greenland's ablation zone to improve projections of mass loss contributions to sea level rise.

TCD
8, 4737–4778, 2014

Bimodal albedo distributions in the ablation zone of the southwestern GrIS

S. E. Moustafa et al.

1 Introduction

Surface albedo, a key variable controlling Greenland Ice Sheet (GrIS) surface melting, is defined as the ratio of reflected to incident solar radiation upon a given surface (Schaepman-Strub et al., 2006). During the melt season, surface albedo modulates absorbed solar radiation at the ice surface, and consequently, the surface energy and mass balance of the ice sheet (Cuffey and Paterson, 2010). Over the last decade, an observed decline in albedo has been linked to enhanced snow grain metamorphic rates from atmospheric warming, and amplified by the melt-albedo feedback (Box et al., 2012; Stroeve et al., 2013; Tedesco et al., 2011). This positive feedback entails snow grain growth owing to melt, reducing surface albedo, thereby increasing solar radiation absorption, and thus, accelerating melt further (Box et al., 2012; Tedesco et al., 2011).

The GrIS surface has a wide range of surface types with different albedos, including snow, ice, dust and sediment-covered ice, cryoconite holes, melt-ponds and streams. Yet, the importance of these surface types on ablation zone albedo, and thus, meltwater production over the melt season is still relatively unresolved, unquantified, and excluded in surface mass balance (SMB) models (Rennermalm et al., 2013). Understanding the distribution of surface types on changing ablation zone albedo is increasingly important due to enhanced surface melt in 2007–2012 associated with anomalously warm atmospheric circulation patterns (Hall et al., 2013; Nghiem et al., 2012; Tedesco et al., 2013) as well as the deposition and accumulation of light-absorbing impurities from snow-free areas and forest fires (Dumont et al., 2014; Keegan et al., 2014).

Large-scale decline in albedo has been greatest in southwest Greenland (−0.04 to −0.16 per decade trend in June and August, respectively; Stroeve et al., 2013). This is related to stronger warming trends (2–4 °C in some regions; Hanna et al., 2014), early melt onset, lack of wintertime accumulation (van den Broeke et al., 2008), expansion of bare ice area (Tedesco et al., 2011), high concentration of impurities (cryoconite, dust, and soot), melting of outcropped ice layers (Wientjes and Oerlemans, 2010; Wientjes et al., 2011), and enhanced meltwater production and runoff (e.g., Mernild et al., 2012).

Seasonal changes in the distribution of different surface types in southwest Greenland's ablation zone have considerable influence on the spatiotemporal variability of surface albedo (Chandler et al., 2014; Knap and Oerlemanns, 1996; Konzelmann and Braithwaite, 1995). During the melt season, surface albedo decreases as cryoconite hole coverage increases (Chandler et al., 2014), melt ponds and supraglacial rivers form efficient drainage networks (Lampkin and VanderBerg, 2013; Kang and Smith, 2013; Smith et al., 2014), and impurities accumulate from exposure of the underlying ice surface (Wientjes and Oerlemans, 2010). Albedo in western Greenland's ablation zone averages around ~ 0.41 for the duration of the melt season (Wientjes et al., 2011), but can vary between > 0.80 for fresh snow, to 0.30–0.60 for bare ice (Cuffey and Patterson, 2010), and ~ 0.10 for cryoconite surfaces (Bøggild et al., 2010; Chandler et al., 2014; Knap and Oerlemans, 1996). Furthermore, negative albedo trends since 2000 (Box et al., 2012) are linked to a darkening of the ice surface from increased surface coverage of meltwater, cryoconite holes, and impurity-rich surface types (Bøggild et al., 2010; Chandler et al., 2014; Wientjes and Oerlemans, 2010).

Changes in surface albedo are typically characterized from the MODerate Resolution Imaging Spectroradiometer (MODIS) and the Advanced Very High Resolution Radiometer (AVHRR) satellite sensors (e.g., Chandler et al., 2014; Stroeve et al., 2013; Wang et al., 2012; Wright et al., 2014) or modeled with regional climate models (RCMs) such as Regional Atmospheric Climate Model (RACMO2; Van Meijgaard et al., 2008) and Modèle Atmosphérique Régional (MAR; Fettweis, 2007). Remotely-sensed and modeled albedo has been validated with ground measurements from dispersed Greenland Climate Network Automatic Weather Stations (GC-Net AWS; Knap and Oerlemans, 1996; Steffen and Box, 2001). These comparisons reveal that satellite products provide reasonable albedo estimates (Box et al., 2012; Stroeve et al., 2005, 2006, 2013), but RCM surface albedos remain physically unrealistic, particularly in bare ice regions like southwest Greenland (Fettweis et al., 2011; Fitzgerald et al., 2012; Rae et al., 2012; Van Angelen et al., 2012). This is attributed to its relatively smooth terrain (Ettema et al., 2010), and poor bare ice and impurity albedo schemes (Alexander et al.,

TCD
8, 4737–4778, 2014
Bimodal albedo distributions in the ablation zone of the southwestern GrIS
S. E. Moustafa et al.

2014), resulting in large inter-model differences in runoff (42 % variance; Vernon et al., 2013). Recent ground albedo observations and snow model simulations of impurity-rich surfaces suggest that incorporating seasonal changes in the albedo distribution of distinct surface types would improve accuracy of modeled meltwater runoff (Chandler et al., 2014; Dumont et al., 2014; Keegan et al., 2014) and GrIS sea level rise contributions (Rennermalm et al., 2013). These findings point to the importance of a detailed assessment of high spectral, spatial, and temporal resolution albedo data to quantify how different surface types control ablation zone albedo, and therefore, melt.

Here, we investigate how ice sheet surface types influence surface albedo and melting by analyzing a new in situ surface albedo dataset, MODIS albedo, and summer seasonal changes in surface type coverage reported in literature. High-quality in situ spectral albedo ground measurements were collected three times during the early 2013 melting season along a fixed transect in the GrIS ablation zone. Only a few studies have collected similar measurements in central and northeast Greenland (e.g., Bøggild et al., 2010; Wright et al., 2014). Our albedo transects were compared with continuous surface albedo measurements collected via automatic weather stations situated at each end of the transect, and MODIS daily albedo (MOD10A1) data. Albedos for distinct surface types were identified in the in situ dataset, and were combined with surface type's fractional area from a nearby site (1030 m a.s.l.; reported by Chandler et al., 2014) to estimate seasonal changes in the albedo distribution. These distributions were compared with seasonal changes in albedo distributions derived from MOD10A1. Finally, the changing albedo and surface type coverage's impact on surface melt in southwest Greenland's ablation zone was quantified and compared with ablation stake measurements installed along the transect. Viewed collectively, these albedo measurements provide a detailed first assessment of the overall frequency distribution, spatiotemporal variability, and ablation rates associated with dominant surface types in southwest Greenland's ablation zone. To the authors' knowledge, the present study is the first high spatial, temporal, and spectral resolution albedo dataset collected in the southwestern GrIS ablation zone.

TCD
8, 4737–4778, 2014

2 Study site description

The study site is located on the southwestern GrIS approximately 30 km northeast of Kangerlussuaq, Greenland (Fig. 1). Albedo measurements were collected along a 1.25 km transect situated between ∼ 510 to 590 m a.s.l., well within the ablation zone for this region (mean equilibrium line altitude of 1553 m a.s.l.; van de Wal et al., 2012). Two meteorological stations, referred to as Base and Top Met Stations, were installed near the transect end points by Site E and A, respectively (Fig. 1) to derive independent measurements of in situ broadband albedo (300–1100 nm), hereafter α_{base} and α_{top}. In addition, ablation stakes were installed at five sites along the albedo transect to measure ice surface ablation rates. Ice sheet surface types examined included white ice, shallow supraglacial streams, and dirty ice, where dirty ice was qualitatively distinguished from white ice based on visible surface sediments. A few small melt ponds (< 1 km^2) were observed in the study area, but likely not in sufficient quantity to explain discrepancies between in situ and MODIS albedo-derived estimates.

3 Methods

3.1 Field spectroscopy measurements

High spatial (∼ 10 m posting), temporal (1–2 days), and spectral (1 nm) resolution spectral albedo measurements, hereafter α_{ASD}, were measured at 325–1075 nm using an ASD Fieldspec HandHeld 2 Spectroradiometer (PANalytical, formerly ASD Inc.), fitted with a Remote Cosine Receptor (RCR) foreoptic. The ASD was mounted on a tripod at 0.4 m distance, and with no foreoptic attached, had a 25° field-of-view, corresponding to a spot size of ∼ 1.1 m on the surface.

Spectral albedos were measured along the transect starting at Site E and ending at Site A on 16, 17, 19, 21, 24, and 25 June, 2013 between 10:00 and 18:00 LT (12:00–20:00 GMT). As will be shown in Sect. 3.4, after rigorous quality control, only transect

TCD
8, 4737–4778, 2014

observations made on the 16, 19, and 25 June were used in analyses. At the start of each transect, the ASD was calibrated to current hemispherical atmospheric conditions by orienting the RCR skyward, along a nadir-viewing angle. Subsequent measurements were taken with the ASD rotated 180° to view the ice surface. Under changing sky conditions, the instrument was recalibrated. Each transect consisted of ~ 100 sample locations, roughly 10 m apart. Despite changing ice conditions rapidly deteriorating temporary location markers, global positioning system (GPS) locations reveal that sample sites in consecutive transects were gathered in close proximity (Fig. 1). Sample sites along the transect were selected based on distance. If a spectrum site intersected with a stream, melt pond, or cryoconite hole, the nearest ice surface was sampled instead. To capture spectral albedo of different ice surface types, separate measurements of streams, dirty ice, and white ice were collected. At each sample location, five consecutive spectra were recorded and averaged. Apparent outliers and physically unrealistic albedo spectra (> 1.0) were removed from the dataset. Broadband α_{ASD} were calculated by averaging albedo over its entire spectral range at each site along the transect. These measurements were compared with MOD10A1 and meteorological station data, as described in Sect. 3.3.

3.2 Continuous broadband albedo measurements at meteorological stations

The Top Met Station was installed upon a homogenous white ice surface, and the Base Met Station was installed above a heterogeneous surface of mixed white and dirty ice. Both stations measured solar radiation fluxes every 0.5 h at 300–1100 nm, using S-LIB-M003 silicon pyranometers and a U30 data logger (Table 1; ±5 % or 10 W m^{-2} precision; Onset Computer Corp., 2010) from 8–26 June. Sensors were attached to a pole drilled into the ice at 1.5 m above the surface, and were kept relatively constant at this height, but occasionally tilted off-level. The Top Met station was re-drilled and installed at 0.5 m height after a period of heavy melting.

Daily average broadband albedo was computed using shortwave flux measured at SZAs < 70° (Stroeve et al., 2005) to minimize the cosine response error inherent to the pyranometers (uncertainty increases by ±5 % for SZAs > 70° ; Onset Computer Corp., 2010). Expected accuracy of α_{base} and α_{top} is ±10 % based on the intrinsic accuracy and cosine response error of the pyranometers. Additional sources of error not quantified here include: meteorological station tilt (e.g., van den Broeke et al., 2004), tower shadowing, and surface roughness effects on measured surface albedo.

3.3 MODIS albedo data

Daily MODIS broadband albedo (300–3000 nm) was acquired from the MOD10A1 product (Version 005) from NASA's Terra satellite (Hall et al., 2006; Klein and Stroeve, 2002). High-quality flagged MOD10A1 albedo data (periods of high SZA and cloudiness were excluded; Schaaf et al., 2011) from 31 May to 30 August 2013 were used in two analyses. First, MOD10A1 albedo corresponding to the transect site (Fig. 1), hereafter $\alpha_{\text{MOD Pixel 1}}$ and $\alpha_{\text{MOD Pixel 2}}$, were compared with observations as described in Sect. 3.3. Second, distributions of MOD10A1 albedo were examined at four spatial extents as described in Sect. 3.6.

Broadband $\alpha_{\text{MOD Pixel 1}}$ and $\alpha_{\text{MOD Pixel 2}}$ were compared with α_{ASD}, α_{base} and α_{top}. Although the three albedo products are calculated over different wavelength ranges, and not expected to match 1 : 1, they should provide similar results. High-quality broadband (325–1075 nm) α_{ASD} data within pixels 1 and 2, hereafter $\alpha_{\text{ASD Pixel 1}}$ and $\alpha_{\text{ASD Pixel 2}}$, were averaged together to indirectly validate $\alpha_{\text{MOD Pixel 1}}$ and $\alpha_{\text{MOD Pixel 2}}$ data, and to facilitate comparison between in situ and remotely-sensed observations.

3.4 Quality-control of α_{ASD} data

To ensure a high-quality α_{ASD} dataset, an impact assessment of variable cloud conditions (i.e., irregular lighting due to transient clouds) and high SZAs during late afternoon albedo transect collections were made. Key et al. (2001) reported a 4–6 % increase in albedo, on average, under cloudy conditions. Albedo readings have also been reported as unreliable at SZAs beyond 70°, due to an increase in diffuse radiation reaching the ice surface (Schaaf et al., 2011; Stroeve et al., 2005, 2013; Wang et al., 2012).

As a proxy for cloud cover, relative cloud cover, hereafter CC, was calculated as the ratio of modeled clear-sky and observed incoming solar radiation similar to Box (1997). "Clear-sky" incoming shortwave fluxes at the surface were calculated with a solar radiance model (Iqbal, 1988). Model inputs of water vapor content, surface pressure, aerosol optical depth at 380 and 500 nm, and ozone optical thickness were estimated from the Kangerlussuaq AEROsol Robotic NETwork (AERONET) station (Holben et al., 2001). SZA was also modeled with the solar radiance model using latitude, longitude, time of day, and day of year information at the Base Met Station. α_{ASD} collected under high CC variability and SZAs approaching extreme angles were subsequently removed. Filtering α_{ASD} data under these criteria ensured the production of a high-quality dataset necessary for subsequent analysis.

Cloud cover and radiative conditions varied among transects (Fig. 2). The majority of α_{ASD} measurements were made at small SZAs (~ 10:30–12:00 LT), except on 21 and 24 June, when observations were made in late afternoon (15:30–16:30 and 16:40–17:50 LT, respectively). Incoming solar radiation fluxes exhibited considerable diurnal variability (average $662 \pm 83\,\mathrm{W\,m^{-2}}$). Outgoing solar radiation displayed similar variability at lower magnitudes (average $239 \pm 18\,\mathrm{W\,m^{-2}}$) during transect dates. CC simulations reveal daily variability in cloud conditions roughly consistent with incoming solar radiation observations, yet on average, remained low (~ 0.13). Half-hourly α_{base} and α_{top} observations changed linearly with SZA, yet remained fairly stable during transect times (Fig. 3a). Above 80° SZA, half hourly α_{base} and α_{top} variability increased, confirming that 70° SZA was a suitable threshold for daily average albedo calculations. Installation tilt likely contributed locally to "unstable" α_{base} observations at higher SZAs. Similarly, a hysteresis observed in α_{top} observations (Fig. 3a) is attributed to a low installation height (0.5 m). These effects can compromise the accurate representation of illumination and viewing geometries, resulting in reduced albedo estimates at high

SZAs (Kuhn, 1974; Wang et al., 2012; Dumont et al., 2012). As such, Top Met Station measurements, and α_{base} at SZAs greater than 70°, were excluded.

High CC variability, instead of consistently high CC, was found to be responsible for saturating α_{ASD} readings on 17, 21, and 24 June (Fig. 3b, only α_{base} shown due to a high hysteresis present in α_{top}). Continuous recalibration of the ASD instrument on 17 and 24 June was inadequate to overcome variable lighting conditions resulting in saturated α_{ASD} readings ($\alpha > 1$). During 21 June, α_{ASD} data did not saturate despite variable sky conditions (0.01–0.52 CC range). Variable cloud conditions on 17, 21, and 24 of June effectively reduced the amount of downwelling longwave radiation relative to shortwave radiation available at the surface, of which, the net effect results in a larger portion of solar radiation available to be reflected by the ice surface (Grenfell and Perovich, 2004; Román et al., 2010; Wang et al., 2012). This can translate to an increase in spectral albedo estimates by ~ 0.06 over active melting ice surfaces (Grenfell and Perovich, 2004).

Despite the shortcomings and uncertainties identified in transect radiative and surface conditions, a high-quality albedo dataset was produced. Optimal SZA, CC, and radiative conditions were observed for 16, 19 and 25 June. α_{ASD} data collected on 17, 21, and 24 June were identified as low-quality based on their dependence on SZA, CC variability, and issues with albedo saturation, and subsequently removed from further analysis (Fig. 3). High-quality α_{ASD} and α_{base} and α_{top} data agree reasonably well (Fig. 4). As much as 40 % of α_{ASD} variance is explained by α_{base} and α_{top}, and the linear regression model slope between the two datasets is close to one ($\alpha_{ASD} = 0.77\alpha_{MET} + 0.14$, where α_{MET} and α_{ASD} are X and Y, respectively and α_{MET} is α_{base} and α_{top} combined). The discrepancy is likely due to differences in exact sample locations and instrumentation. Tables 2 and 3 provide summary statistics related to high-quality α_{ASD} and transect conditions.

TCD
8, 4737–4778, 2014

3.5 Ablation and albedo at dominant surface types

Surface melting between 8–26 June was estimated using ablation stakes installed at five sites across the albedo transect, hereafter $M_{\text{stake}XY}$, where X denotes Sites A–E, and Y denotes surface type – white ice (W), dirty ice (D), or shallow 5–10 cm deep streams (S) (Fig. 1). Bamboo poles were used as stakes (Hubbard and Glasser, 2005), and ablation rates were recorded every 1–3 days by measuring the distance between the bamboo pole top and ice sheet surface at cm-scale resolution.

Albedos of white ice at Sites A, B, and C, hereafter $\alpha_{\text{ASD\_AW}}$, $\alpha_{\text{ASD\_BW}}$, and $\alpha_{\text{ASD\_CW}}$, were estimated by averaging visible (400–700 nm) α_{ASD} observations made within 10 m of stakes for each transect date. At Sites D and E, albedos of white and dirty ice, hereafter $\alpha_{\text{ASD\_DW}}$, $\alpha_{\text{ASD\_DD}}$, $\alpha_{\text{ASD\_EW}}$, and $\alpha_{\text{ASD\_ED}}$, were estimated from the bimodal distribution of α_{ASD} observations made within 10 m of stakes for each transect date. Stream albedo, hereafter α_{stream}, was determined from occasional α_{ASD} measurements at various shallow surface streams between 13–25 June. Cryoconite hole albedo, hereafter α_{cryo}, was parameterized using published values of Bøggild et al. (2010).

3.6 Melt season albedo distributions

Two types of melt season albedo distributions were constructed: (1) computed distributions based on α_{ASD} for distinct surfaces and fractional surface coverage area from Chandler et al. (2014); and (2) observed MODIS-derived distributions.

The computed distributions were constructed by assuming that the albedo distribution for each distinct surface is represented by a normal distribution $N(\overline{x}, s)$, with $\overline{x} = \overline{\alpha_{\text{ASD}}}$ representing surface type and standard deviation, s, fixed to 0.09. Four distributions were constructed: white ice $N(0.68, 0.09)$, dirty ice $N(0.23, 0.09)$, shallow streams $N(0.26, 0.09)$, and cryoconite holes $N(0.10, 0.09)$. Relative surface coverage of these four dominant surface types was derived at five distinct time periods (1 June, 19 June, 18 July, 28 July, and 5 August) over the 2012 melt season from Chandler et al. (2014) to represent transient ice surface conditions, classified here as "early

TCD
8, 4737–4778, 2014

summer ice", "dirty ice exposure", "melt", "darkening ice", and "late summer ice", respectively. A composite distribution for each distinct time step was calculated as the weighted mean of surface type distributions, where the weights were determined by their relative surface coverage area. Since Chandler et al. (2014) data is from 2012, results were not directly comparable with 2013 MOD10A1 data, but should capture melt season evolution.

To validate the computed distributions, high-quality MOD10A1 data were used to construct observed albedo distributions at four spatial scales (20 × 20, 50 × 50, 100 × 100, and 150 × 150 pixel extents; Fig. 1). The spatial resolution of the original MOD10A1 data is 463 m, corresponding to study areas of 9.3, 23.2, 46.3, and 69.5 km^2 for the four spatial extents, respectively. Using a kernel smoothing density estimator, the average probability density distribution was computed at 0.01 albedo bin widths (range from 0.05 to 1). The seasonal average albedo distribution was calculated at the four spatial scales, and five-day average albedo distributions were calculated for the 100 × 100 pixel scale.

3.7 Computation of relative melt rates

Relative surface melt rates were computed using the net solar radiation equation (assuming net longwave radiation terms are negligible), using observed values of incoming solar radiation from the Base Met Station on 16, 19, and 25 June, and visible albedo values for computed and observed distribution methods. Net solar radiation (E_R) varies as a function of incoming solar radiation ($E_S^{\downarrow}$) and albedo (α_s), where units of energy are represented as $W\,m^{-2}$:

$$E_R = E_S^{\downarrow}(1 - \alpha_s) \quad (1)$$

(Cuffey and Patterson, 2010). Melt rate, defined as the heat needed to melt snow/ice when near-surface temperatures are ≥ to 0 °C, was computed in units of $m\,s^{-1}$:

$$M = (E_R \cdot \Delta t)(L_f \cdot \rho_w)^{-1} \quad (2)$$

where Δt is the time interval (s); L_f is latent heat of fusion (3.34×10^5 J kg^{-1}); and ρ_w is density of water (1000 kg m^{-3}). Since the meteorological station datasets lack surface energy balance terms required to compute the entire energy budget, calculating absolute melt rates was not possible. Instead, the percent difference in estimated melt rates was computed for each distribution relative to the early melt season ablation rates (mean of 3.50×10^{-7} m s^{-1} for "early summer ice" computed distribution; mean of 2.31×10^{-7} m s^{-1} for 31 May to 4 June observed MODIS distribution).

4 Results

4.1 Spatiotemporal patterns in ablation zone albedo

Spatial variability of α_{ASD} along the transect follows a consistent pattern on all three dates, averaging low values (0.55 ± 0.06) the first ~300 m, followed by increased albedo, reaching a plateau of 0.74 ± 0.09 at ~600 m, and remaining nearly constant with the exception of a dip to 0.48 ± 0.02 at ~900 m (Fig. 5a). While individual α_{ASD} sites exhibit high day-to-day variability (Fig. 5a), data averaged in 50 m bins covary spatially along the transect gradient (Fig. 5b). α_{ASD} spatial range is considerable and varies between a minimum of 0.15 (25 June) and a maximum of 0.86 (16 June; Table 2). α_{base} and α_{top} are distinctly different on the three transect dates (Fig. 6). For instance, on 16 June, daily average albedo ranged from 0.40 to 0.64 (difference of 0.24), while on 25 June ranged from 0.32 to 0.54 (difference of 0.22) at α_{base} and α_{top}, respectively (Table 2). The high spatial variability in α_{ASD} over short distances is indicative of the heterogeneous surface that characterizes the field site and surrounding ablation zone, not necessarily captured in α_{base} and α_{top} observations.

Temporal variability in daily average α_{base} and α_{top} follows an uneven decline from 8–26 June, with α_{base} consistently ~0.2 lower than α_{top} (Fig. 6). This general decline is observed through the entire melting season by $\alpha_{MOD\ Pixel\ 1}$ and $\alpha_{MOD\ Pixel\ 2}$. The MOD10A1 albedo time series illustrates an inconsistent reduction in albedo of the ice surface, averaging 0.29 on 28 June and 0.43 on 14 August. Fresh snow fell on ∼ 18 August, abruptly increasing MOD10A1 albedo to above 0.75. High-quality, pixel-averaged daily broadband $\alpha_{\text{ASD Pixel 1}}$ and $\alpha_{\text{ASD Pixel 2}}$ confirm the general darkening observed in α_{base} and α_{top}, $\alpha_{\text{MOD Pixel 1}}$ and $\alpha_{\text{MOD Pixel 2}}$. While absolute magnitudes among the three ground- and satellite-derived albedo products diverge due to sensor and spatial resolution differences, temporal variability show general agreement.

Albedos of dirty and white ice surfaces are distinctly different for each ablation stake site (Table 4). This is illustrated by the clear separation between high and low albedo distributions of visible α_{ASD} within 10 m radius of ablation stake sites D and E, where both dirty and white ice surface are observed (Fig. 7). A threshold of 0.5 was used to separate darker and lighter surfaces at Sites D and E (white surfaces included $\alpha_{\text{ASD\_DW}}$ and $\alpha_{\text{ASD\_EW}}$; dark surfaces included $\alpha_{\text{ASD\_DD}}$, $\alpha_{\text{ASD\_ED}}$, α_{stream}, and α_{cryo}).

Ablation rates are typically higher for dark surfaces (dirty ice and streams) than light surfaces (white ice; Fig. 8). White ice surfaces have higher visible α_{ASD} values (mean of 0.69), corresponding to lower average ablation rates (5.80×10^{-7} m s^{-1}). In contrast, dirty ice and stream surfaces have lower mean visible α_{ASD} values (0.26), corresponding to higher average ablation rates (7.00×10^{-7} m s^{-1}). The observed mean difference between white and dark surface ablation rates is 2.31×10^{-7} m s^{-1}. Melt rate calculations (Eqs. 1 and 2) resulted in higher average ablation rates (3.50×10^{-7} m s^{-1} for white surfaces and 7.00×10^{-7} m s^{-1} for dark surfaces, corresponding to a mean difference of 4.63×10^{-7} m s^{-1}). Differences between observed and calculated melt rates could be due ablation stake measurement errors and simplification of calculations (e.g., no consideration of longwave radiation). Regardless of this, relative melt rates between light and dark surfaces are captured by the calculations, and thus useful for investigating seasonal melt rate changes as described next.

The spread in observed white ice visible albedo values results in greater variability in observed ablation rate estimates (Fig. 8). In contrast, minimal visible albedo variability is observed for dirty ice and stream surfaces. As such, grouping these two ice surface types into a "darker surface" type classification is justified. Differences in ablation rates for stream surfaces are due to a lack of albedo data. While ablation rates were measured at several ablation stake stream sites, only occasional α_{ASD} measurements were collected over these surfaces. Considerable spread in ablation rates for stream observations could be explained by varying stream depth (Legleiter et al., 2014). The depth of these ice streams determines the attenuation and scattering of radiant energy, thereby influencing the observed albedo measurements.

4.2 Melt season albedo distributions

Computed albedo frequencies reveal a bimodal distribution as the melt season progresses (Fig. 9). The relative strength of the first and secondary modes change as the fractional area of darker surfaces expands from "dirty ice exposure" to "melt" distributions and onwards. At the start of the melt season, the abundance of lighter surfaces coincides with a higher probability of high visible α_{ASD} values. As darker surfaces progressively populate the ablation zone with the onset of the melt season, computed albedo distributions predict a concomitant higher probability of lower albedo. Thus, there is an apparent dichotomy between darker and lighter surfaces "competing" to control the overall albedo distribution of the ablation zone. A transition towards a left-skewed distribution is likely due to darker surfaces shifting the overall distribution to lower albedo values, and is confirmed by high-quality visible α_{ASD} distributions (Fig. 10). Relative melt rates increase sharply (by 41.8 ± 2.7 %) from "dirty ice exposure" to "melt", coinciding with a strengthening of the second, lower mode in the computed albedo distribution (Fig. 11).

Observed MOD10A1 albedo distributions at four spatial extents (Fig. 12) reveal that the computed bimodal distribution above (cf. Fig. 9) is manifested in reality. While the spatial extent of the MOD10A1 sample influences the seasonal average albedo distribution, two distinct surface types – dark and light surfaces – dominate the seasonal signal (Fig. 12). At the smallest spatial scale (20 × 20 – i.e., 9.3 km^2), lower albedos from darker surfaces of the lower ablation zone control the density distribution, while at the largest spatial scale (150 × 150 – i.e., 69.5 km^2), the probability distribution is

TCD
8, 4737–4778, 2014

primarily influenced by higher albedos from lighter surfaces (e.g., snow) of the upper ablation zone.

MOD10A1 albedo at the 100 × 100 (i.e., 46.3 km^2) spatial scale transitions from a high, unimodal distribution at the start of the melt season (31 May to 4 June), to a bimodal distribution mid-melt season (20–24 June), and shifts abruptly to a new, low unimodal distribution peak melt season (30 July to 3 August; Fig. 13). The abrupt shift from a lighter- to darker-dominated surface corresponds to an observed melt rate percent difference increase of 51.6 % between 10–14 July and 20–24 July pentad average albedo distributions (Fig. 14).

5 Discussion

GrIS's ablation zone albedos are strongly influenced by the presence or absence of impurity-rich debris on its surface. White ice and dust-covered ice have distinctly different albedos, resulting in a left-skewed albedo distribution at the end of June. This suggests that an abrupt switch from high to low albedo can be triggered by a modest melt event, resulting in amplified melt rates. This pattern is supported by computed and remotely-sensed albedo distributions, revealing that a bimodal distribution develops seasonally, with two alternate states. A modest melt event can trigger a sudden switch from a high to low albedo mode, resulting in augmented ablation rates. These findings suggest that a shift in dominant surface type from white ice to impurity-rich ice surfaces is an important driver in increasing seasonal ice sheet melt rates.

The first quality-controlled in situ ablation zone albedo dataset collected along a 1.25 km transect during three days in June 2013 is presented. Albedo data collected during in situ transect dates resemble an early summer ice surface classified in Chandler et al. (2014) and Knap and Oerlemans (1996; Fig. 6). Here, remaining snow cover and superimposed ice gradually melts, revealing underlying impurities and last ablation season's cryoconite holes. This period corresponds to an unsteady decrease in albedo (Fig. 6) primarily due to fluctuations in diurnal shortwave fluxes, which is responsible

TCD
8, 4737–4778, 2014

for the activation and development of an efficient surface meltwater routing system, and increase in cryoconite hole coverage (Chandler et al., 2014). Accumulation of exposed below-surface impurities (Wientjes and Oerlemans, 2010) mitigates the rate of change in ablation zone albedo. Turbulent sensible heat fluxes from adjacent pro-glacial areas may function as an alternative explanation for the non-linear decline in ground albedo measurements, serving to limit the melt-albedo feedback's influence (van den Broeke et al., 2011).

An increase in debris-rich and stream surfaces over the melting season (Fig. 9) is likely responsible for the left-skewed distribution identified in the observed α_{ASD} distribution (Fig. 10). Under the assumptions that distinct surface types follow a normal distribution, a bimodal probability distribution preferentially develops as ablation zone albedo decreases rapidly over the melt season due to development of an efficient meltwater drainage system, increase in cryoconite hole coverage, and accumulation of debris-rich sediments (Fig. 9). The observed albedo distributions reveal abrupt shifts in the seasonal albedo distribution (Fig. 13). At certain spatial scales, these albedo distributions transition from a high- to low-dominated mode (Fig. 12), enabling enhanced melt rates (Figs. 11 and 14). Alexander et al. (2014) also observed bimodal albedo distributions for Greenland's ablation zone by analyzing MAR and MODIS products between 2000–2013. In contrast to this study, Alexander et. al. (2014) attributes the dominant modes to the presence of snow and ice (and firn). This discrepancy could be due to the larger study area in Alexander et al. (2014), which may include areas unaffected by dust deposition and outcropped ice layers.

The bimodal albedo distribution and shift from a higher to a lower albedo mode (Figs. 9 and 13) indicate that a switch in dominant surface type (i.e., from light to dark) during the melt season, and not solely grain size metamorphism, as suggested in Box et al. (2012) and Tedesco et al. (2011), are largely responsible for lowering ablation zone albedo. Furthermore, transition from a light- to dark-dominated surface is abrupt rather than gradual. Consistent with Chandler et al. (2014), the initial drop in ablation zone albedo is likely due to the transition from dry to wet, and patchy snow surfaces,

TCD
8, 4737–4778, 2014

while successive lowering of albedo is predominantly due to an increase in darker surface area coverage (e.g., cryoconite holes, accumulation of impurities, and stream organization), where the darker, lower albedo surface mode dominates. These distributions correspond to percent differences in melt rate estimates that are substantial over the melt season (Figs. 11 and 14), and highlight the importance of considering the albedo of ablation zone surface types.

Plausible scenarios of future atmospheric warming, excess deposition of light-absorbing impurities (Dumont et al., 2014) and black carbon from increased forest fire frequency or incomplete fuel combustion (Keegan et al., 2014), will likely result in earlier and abrupt shifts in ablation zone albedo's distribution, contributing to amplified surface melting, and thus, enhanced mass loss. These effects will likely be exacerbated in southwest Greenland's ablation zone, where continued negative albedo trends (Stroeve et al., 2013), and increasingly warmer average summer temperatures (Keegan et al., 2014), in conjunction with bare ice, light-absorbing impurities, and cryoconite holes, are expected to dominate.

6 Conclusions

A first high-quality in situ spectral albedo dataset collected along a fixed transect is presented for southwest Greenland's ablation zone. Previous studies have attributed snow grain metamorphism and ice-albedo feedback as primary mechanisms for lowering ablation zone albedo; however, these data suggest that a bimodal distribution and consequentially, an abrupt shift from light to dark-dominated surfaces, characterize seasonal changes in Greenland's ablation zone, and therefore, melt rates. This research provides a new understanding of ablation zone albedo distributions of distinct surface types, and their modulation of surface ablation.

Continued atmospheric warming coinciding with a darkening ice surface will alter the distribution of dominant surface types in Greenland's ablation zone. A shift in Greenland's ablation zone albedo distribution, and addition of impurities to its surface, will amplify surface melt and thus, mass loss, of which these processes are not currently realized in SMB models. Future modeling efforts should consider incorporating the effects and evolution of dominant surface types on ablation zone albedo for improved simulation of surface melting and runoff from the southwestern GrIS ablation zone.

Acknowledgements. S. E. Moustafa, A. K. Rennermalm, L. C. Smith and J. R. Mioduszewski were funded by NASA grant NNX11AQ38G. S. E. Moustafa was also funded by NASA Earth and Space Science Fellowship Program NNX12AN98H. Additional funding was provided by Rutgers University Faculty Research Grant. The authors would like to thank L. S. Koenig for valuable feedback and commentary.

References

Alexander, P. M., Tedesco, M., Fettweis, X., van de Wal, R. S. W., Smeets, C. J. P. P., and van den Broeke, M. R.: Assessing spatio-temporal variability and trends (2000–2013) of modelled and measured Greenland ice sheet albedo, The Cryosphere Discuss., 8, 3733–3783, doi:10.5194/tcd-8-3733-2014, 2014.

Bøggild, C. E., Brandt, R. E., Brown, K. J., and Warren, S. G.: The ablation zone in northeast Greenland: ice types, albedos and impurities, J. Glaciol., 56, 101–113, doi:10.3189/002214310791190776, 2010.

Box, J. E., Fettweis, X., Stroeve, J. C., Tedesco, M., Hall, D. K., and Steffen, K.: Greenland ice sheet albedo feedback: thermodynamics and atmospheric drivers, The Cryosphere, 6, 821–839, doi:10.5194/tc-6-821-2012, 2012.

Chandler, D. M., Alcock, J. D., Wadham, J. L., Mackie, S. L., and Telling, J.: Seasonal changes of ice surface characteristics and productivity in the ablation zone of the Greenland Ice Sheet, The Cryosphere Discuss., 8, 1337–1382, doi:10.5194/tcd-8-1337-2014, 2014.

Cuffey, K. and Paterson, W. S. B.: The Physics of Glaciers, 4th Edn., Elsevier Inc., Burlington and Oxford, 2010.

Dumont, M., Gardelle, J., Sirguey, P., Guillot, A., Six, D., Rabatel, A., and Arnaud, Y.: Linking glacier annual mass balance and glacier albedo retrieved from MODIS data, The Cryosphere, 6, 1527–1539, doi:10.5194/tc-6-1527-2012, 2012.

Dumont, M., Brun, E., Picard, G., Michou, M., Libois, Q., Petit, J., Geyer, M., Morin, S., and Josse, B.: Contribution of light-absorbing impurities in snow to Greenland's darkening since 2009, Nat. Geosci., 7, 509–512, doi:10.1038/ngeo2180, 2014.
Ettema, J., van den Broeke, M. R., van Meijgaard, E., van de Berg, W. J., Box, J. E., and Steffen, K.: Climate of the Greenland ice sheet using a high-resolution climate model – Part 1: Evaluation, The Cryosphere, 4, 511–527, doi:10.5194/tc-4-511-2010, 2010.
Fettweis, X.: Reconstruction of the 1979–2006 Greenland ice sheet surface mass balance using the regional climate model MAR, The Cryosphere, 1, 21–40, doi:10.5194/tc-1-21-2007, 2007.
Fettweis, X., Tedesco, M., van den Broeke, M., and Ettema, J.: Melting trends over the Greenland ice sheet (1958–2009) from spaceborne microwave data and regional climate models, The Cryosphere, 5, 359–375, doi:10.5194/tc-5-359-2011, 2011.
Fitzgerald, P. W., Bamber, J. L., Ridley, J. K., and Rougier, J. C.: Exploration of parametric uncertainty in a surface mass balance model applied to the Greenland ice sheet, J. Geophys. Res., 117, F01021, doi:10.1029/2011JF002067, 2012.
Grenfell, T. C. and Perovich, D. K.: Seasonal and spatial evolution of albedo in a snow-ice-land-ocean environment, J. Geophys. Res., 109, C01001, doi:10.1029/2003JC001866, 2004.
Hall, D. K., Riggs, G. A., and Salomonson, V. V.: MODIS Snow and Sea Ice Products 2006: Earth Science Satellite Remote Sensing – Volume I: Science and Instruments, edited by: Qu, J. J., Gao, W., Kafatos, M., Murphy, R. E., and Salomonson, V. V., Springer, New York, 154–181, 2006.
Hall, D. K., Comiso, J. C., DiGirolamo, N. E., Shuman, C. A., Box, J. E., and Koenig, L. S.: Variability in the surface temperature and melt extent of the Greenland ice sheet from MODIS, Geophys. Res. Lett., 40, 2114–2120, doi:10.1002/grl.50240, 2013.
Hanna, E., Fettweis, X., Mernild, S. H., Cappelen, J., Ribergaard, M. H., Shuman, C. A., Steffen, K., Wood, L., and Mote, T. L.: Atmospheric and oceanic climate forcing of the exceptional Greenland ice sheet surface melt in summer 2012, Int. J. Climatol., 34, 1022–1037, doi:10.1002/joc.3743, 2014.
Holben, N., Tanr, D., Smirnov, A., Eck, T. F., Slutsker, I., Newcomb, W. W., Schafer, J. S., Chatenet, B., Lavenu, F., Kaufman, J., Castle, J. Vande, Setzer, A., Markham, B., Clark, D., Halthore, R., Karneli, A., Neill, N. T. O., Pietras, C., Pinker, T., Voss, K., and Zibordi, G.: An emerging ground-based aerosol climatology?: aerosol optical depth from AERONET, J. Geophys. Res., 106, 12067–12097, 2001.

TCD
8, 4737–4778, 2014
Bimodal albedo distributions in the ablation zone of the southwestern GrIS
S. E. Moustafa et al.

Iqbal, M.: Spectral and total sun radiance under cloudless skies, in: Physical Climatology for Solar and Wind Energy, edited by: Guzzi, R. and Justus, C. G., World Scientific, Singapore, 196–242, 1988.
Keegan, K. M., Albert, M. R., McConnell, J. R., and Baker, I.: Climate change and forest fires synergistically drive widespread melt events of the Greenland Ice Sheet., P. Natl. Acad. Sci. USA., 111, 7964–7967, doi:10.1073/pnas.1405397111, 2014.
Klein, A. G. and Stroeve, J.: Development and validation of a snow albedo algorithm for the MODIS instrument, Annals of Glaciol., 34, 45–52, 2002.
Knap, W. H. and Oerlemans, J.: The surface albedo of the Greenland ice sheet: satellite derived and in situ measurements in the Sendre Stromfjord area during the 1991 melt season, J. Glaciol., 42, 364–374, 1996.
Konzelmann, T. and Braithwaite, R. J.: Variations of ablation, albedo and energy balance at the margin of the Greenland ice sheet, Kronprins Christian Land, eastern north Greenland, J. Glaciol., 41, 174–182, 1995.
Kuhn, M.: Anisotropic reflection from sastrugi fields, Antarc. J. US, 9, 123–125, 1974.
Lampkin, D. J. and VanderBerg, J.: Supraglacial melt channel networks in the Jakobshavn Isbrae region during the 2007 melt season, Hydrol. Process., doi:10.1002/hyp.10085, 2013.
Legleiter, C. J., Tedesco, M., Smith, L. C., Behar, A. E., and Overstreet, B. T.: Mapping the bathymetry of supraglacial lakes and streams on the Greenland ice sheet using field measurements and high-resolution satellite images, The Cryosphere, 8, 215–228, doi:10.5194/tc-8-215-2014, 2014.
Mernild, S. H. and Liston, G. E.: Greenland freshwater runoff. Part II: Distribution and trends, 1960–2010, J. Climate, 25, 6015–6035, doi:10.1175/JCLI-D-11-00592.1, 2012.
Nghiem, S. V., Hall, D. K., Mote, T. L., Tedesco, M., Albert, M. R., Keegan, K., Shuman, C. A., DiGirolamo, N. E., and Neumann, G.: The extreme melt across the Greenland Ice Sheet in 2012, Geophys. Res. Lett., 39, 1–6, doi:10.1029/2012GL053611, 2012.
Onset Computer Corp.: Silicon Pyranometer Smart Sensor (Part # S-LIB-M003), available at: http://wpc.306e.edgecastcdn.net/80306E/onsetcomp_com/files/manual_pdfs/6708-D-MAN-S-LIB.pdf (last access: 14 August 2013), 2010.
Rae, J. G. L., Aðalgeirsdóttir, G., Edwards, T. L., Fettweis, X., Gregory, J. M., Hewitt, H. T., Lowe, J. A., Lucas-Picher, P., Mottram, R. H., Payne, A. J., Ridley, J. K., Shannon, S. R., van de Berg, W. J., van de Wal, R. S. W., and van den Broeke, M. R.: Greenland ice sheet

TCD
8, 4737–4778, 2014

Bimodal albedo distributions in the ablation zone of the southwestern GrIS

S. E. Moustafa et al.

surface mass balance: evaluating simulations and making projections with regional climate models, The Cryosphere, 6, 1275–1294, doi:10.5194/tc-6-1275-2012, 2012.
Rennermalm, A. K., Smith, L. C., Chu, V. W., Box, J. E., Forster, R. R., Van den Broeke, M. R., Van As, D., and Moustafa, S. E.: Evidence of meltwater retention within the Greenland ice sheet, The Cryosphere, 7, 1433–1445, doi:10.5194/tc-7-1433-2013, 2013.
Román, M. O., Schaaf, C. B., Lewis, P., Gao, F., Anderson, G. P., Privette, J. L., Strahler, A. H., Woodcock, C. E., and Barnsley, M.: Assessing the coupling between surface albedo derived from MODIS and the fraction of diffuse skylight over spatially-characterized landscapes, Remote Sens. Environ., 114, 738–760, doi:10.1016/j.rse.2009.11.014, 2010.
Schaaf, C. B., Liu, J., Gao, F., and Strahler, A. H.: Aqua and Terra MODIS albedo and reflectance anisotropy products, in: Remote Sensing and Global Environmental Change, 549–561, Springer, New York, 2011.
Schaepman-Strub, G., Schaepman, M. E., Painter, T. H., Dangel, S., and Martonchik, J. V.: Reflectance quantities in optical remote sensing – definitions and case studies, Remote Sens. Environ., 103, 27–42, doi:10.1016/j.rse.2006.03.002, 2006.
Smith, L. C., Chu, V. W., Yang, K., Gleason, C. J., Pitcher, L. H., Rennermalm, A. K., Legleiter, C. J., Behar, A. E., Overstreet, B. T., Moustafa, S. E., Tedesco, M., Forster, R. R., LeWinter, A. L., Finnegan, D. C., Sheng, Y., and Balog, J.: Supraglacial rivers on the Greenland Ice Sheet, P. Natl. Acad. Sci. USA, in review, 2014.
Steffen, K. and Box, J.: Surface climatology of the Greenland Ice Sheet: Greenland climate network 1995–1999, J. Geophys. Res., 106, 33951–33964, 2001.
Stroeve, J., Box, J. E., Gao, F., Liang, S., Nolin, A., and Schaaf, C.: Accuracy assessment of the MODIS 16-day albedo product for snow: comparisons with Greenland in situ measurements, Remote Sens. Environ., 94, 46–60, doi:10.1016/j.rse.2004.09.001, 2005.
Stroeve, J. C., Box, J. E., and Haran, T.: Evaluation of the MODIS (MOD10A1) daily snow albedo product over the Greenland Ice Sheet, Remote Sens. Environ., 105, 155–171, doi:10.1016/j.rse.2006.06.009, 2006.
Stroeve, J., Box, J. E., Wang, Z., Schaaf, C., and Barrett, A.: Re-evaluation of MODIS MCD43 Greenland albedo accuracy and trends, Remote Sens. Environ., 138, 199–214, doi:10.1016/j.rse.2013.07.023, 2013.
Tedesco, M., Fettweis, X., van den Broeke, M. R., van de Wal, R. S. W., Smeets, C. J. P. P., van de Berg, W. J., Serreze, M. C., and Box, J. E.: The role of albedo and accumulation

Discussion Paper | Discussion Paper | Discussion Paper | Discussion Paper |

in the 2010 melting record in Greenland, Environ. Res. Lett., 6, 014005, doi:10.1088/1748-9326/6/1/014005, 2011.

Tedesco, M., Fettweis, X., Mote, T., Wahr, J., Alexander, P., Box, J. E., and Wouters, B.: Evidence and analysis of 2012 Greenland records from spaceborne observations, a regional climate model and reanalysis data, The Cryosphere, 7, 615–630, doi:10.5194/tc-7-615-2013, 2013.

van Angelen, J. H., Lenaerts, J. T. M., Lhermitte, S., Fettweis, X., Kuipers Munneke, P., van den Broeke, M. R., van Meijgaard, E., and Smeets, C. J. P. P.: Sensitivity of Greenland Ice Sheet surface mass balance to surface albedo parameterization: a study with a regional climate model, The Cryosphere, 6, 1175–1186, doi:10.5194/tc-6-1175-2012, 2012.

van den Broeke, M., van As, D., Reijmer, C., and van de Wal, R.: Assessing and improving the quality of unattended radiation observations in Antarctica, J. Atmos. Ocean. Tech., 21, 1417–1431, doi:10.1175/1520-0426(2004)021<1417:AAITQO>2.0.CO;2, 2004.

van den Broeke, M., Smeets, P., Ettema, J., van der Veen, C., van de Wal, R., and Oerlemans, J.: Partitioning of melt energy and meltwater fluxes in the ablation zone of the west Greenland ice sheet, The Cryosphere, 2, 179–189, doi:10.5194/tc-2-179-2008, 2008.

van den Broeke, M. R., Smeets, C. J. P. P., and van de Wal, R. S. W.: The seasonal cycle and interannual variability of surface energy balance and melt in the ablation zone of the west Greenland ice sheet, The Cryosphere, 5, 377–390, doi:10.5194/tc-5-377-2011, 2011.

Van Meijgaard, E., van Ulft, L. H., Van de Berg, W. J., Bosveld, F. C., Van den Hurk, B., Lenderink, G., and Siebesma, A. P.: The KNMI regional atmospheric climate modelRACMOversion 2.1, Tech. Rep. 302, Royal Netherlands Meteorological Institute, De Bilt, 2008.

van de Wal, R. S. W., Boot, W., Smeets, C. J. P. P., Snellen, H., van den Broeke, M. R., and Oerlemans, J.: Twenty-one years of mass balance observations along the K-transect, West Greenland, Earth Syst. Sci. Data, 4, 31–35, doi:10.5194/essd-4-31-2012, 2012.

Wang, Z., Schaaf, C. B., Chopping, M. J., Strahler, A. H., Wang, J., Román, M. O., Rocha, A. V., Woodcock, C. E., and Shuai, Y.: Evaluation of Moderate-resolution Imaging Spectroradiometer (MODIS) snow albedo product (MCD43A) over tundra, Remote Sens. Environ., 117, 264–280, doi:10.1016/j.rse.2011.10.002, 2012.

Wientjes, I. G. M. and Oerlemans, J.: An explanation for the dark region in the western melt zone of the Greenland ice sheet, The Cryosphere, 4, 261–268, doi:10.5194/tc-4-261-2010, 2010.

Wientjes, I. G. M., Van de Wal, R. S. W., Reichart, G. J., Sluijs, A., and Oerlemans, J.: Dust from the dark region in the western ablation zone of the Greenland ice sheet, The Cryosphere, 5, 589–601, doi:10.5194/tc-5-589-2011, 2011.

Wright, P., Bergin, M., Dibb, J., Lefer, B., Domine, F., Carman, T., Carmagnola, C., Dumont, M., Courville, Z., Schaaf, C., and Wang, Z.: Comparing MODIS daily snow albedo to spectral albedo field measurements in Central Greenland, Remote Sens. Environ., 140, 118–129, doi:10.1016/j.rse.2013.08.044, 2014.

Yang, K. and Smith, L. C.: Supraglacial streams on the Greenland Ice Sheet delineated from combined spectral–shape information in high-resolution satellite imagery, IEEE Geosci. Remote Sens. Lett., 10, 801–805, doi:10.1109/LGRS.2012.2224316, 2013.

TCD

8, 4737–4778, 2014

Bimodal albedo distributions in the ablation zone of the southwestern GrIS

S. E. Moustafa et al.

Table 1. Meteorological station sites and associated variables.

Site	Latitude	Longitude	Elevation (m)	Start Date	End Date
Base Met Station	67.151629	50.027993	511.3	8 Jun	26 Jun
Top Met Station	67.146857	50.001186	586.0	14 Jun	26 Jun

TCD
8, 4737–4778, 2014

TCD
8, 4737–4778, 2014

Table 2. Descriptive statistics for high-quality albedo transects. SZA and CC listed for Base Met Station only.

Transect Date	Start Time	End Time	Min Vis α_{ASD}	Max Vis α_{ASD}	Mean Vis α_{ASD}	Daily Average α_{base}	Daily Average α_{top}	Min SZA (°)	Max SZA (°)	Mean SZA (°)	Min CC	Max CC	Mean CC
16 Jun	10:32:33	11:53:57	0.277	0.859	0.606	0.404	0.636	45.615	50.454	47.828	0.135	0.176	0.157
19 Jun	10:39:30	11:35:59	0.218	0.767	0.546	0.316	0.541	46.449	49.925	48.093	0.045	0.084	0.065
25 Jun	10:20:29	11:11:00	0.151	0.855	0.608	0.333	0.525	47.963	51.525	49.677	0.119	0.138	0.125

Table 3. Summary statistics for high-quality broadband and visible α_{ASD} retrievals by transect date reported as mean $\pm 1\sigma$.

Transect Date	Broadband (325–1075 nm) α_{ASD} mean and standard deviation	Visible (400–700 nm) α_{ASD} mean and standard deviation
16 Jun	0.51 ± 0.096	0.61 ± 0.126
19 Jun	0.48 ± 0.115	0.61 ± 0.161
25 Jun	0.45 ± 0.101	0.55 ± 0.141
All Dates	0.48 ± 0.104	0.59 ± 0.143

TCD
8, 4737–4778, 2014

Table 4. Average visible α_{ASD} within a 10 m radius of ablation stake sites and classified by surface type.

Ablation stake sites	α_{ASD} site average	White surfaces	Dark surfaces
Site A	0.750	–	–
Site B	0.690	–	–
Site C	0.740	–	–
Site D	0.490	0.652	0.274
Site E	0.555	0.635	0.232

TCD
8, 4737–4778, 2014

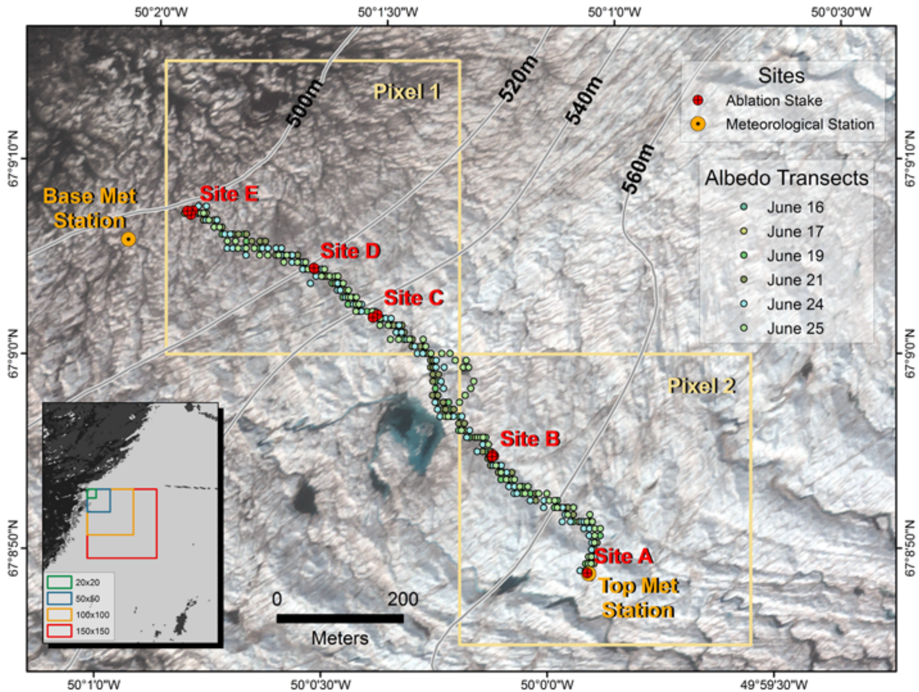

Figure 1. 23 June 2013 WorldView-2 true color image (bands 5, 3, and 2 RGB) of the study site with elevation contours (m), MODIS pixel extents, and location of the six albedo transects, ablation stake, and meteorological station sites. Location of four MODIS spatial extent regions overlaid on a 31 May 2013 MOD10A1 image (black box inset).

TCD
8, 4737–4778, 2014

Bimodal albedo distributions in the ablation zone of the southwestern GrIS

S. E. Moustafa et al.

Title Page
Abstract | Introduction
Conclusions | References
Tables | Figures
◂ ▸
Back | Close
Full Screen / Esc
Printer-friendly Version
Interactive Discussion

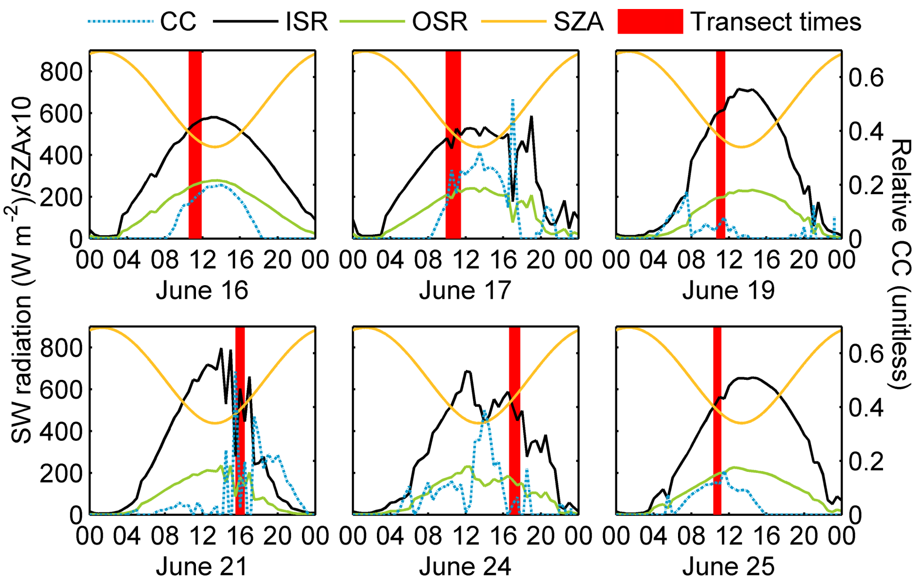

Figure 2. Radiative conditions during transect dates at the Base Met Station, including incoming solar radiation (ISR, black line), outgoing solar radiation (OSR, green line; left *y* axis), modeled relative cloud cover (CC, blue stippled line; right *y* axis), and solar zenith angles (SZA, yellow line; left *y* axis). Red shaded regions show α_{ASD} data collection times.

TCD
8, 4737–4778, 2014

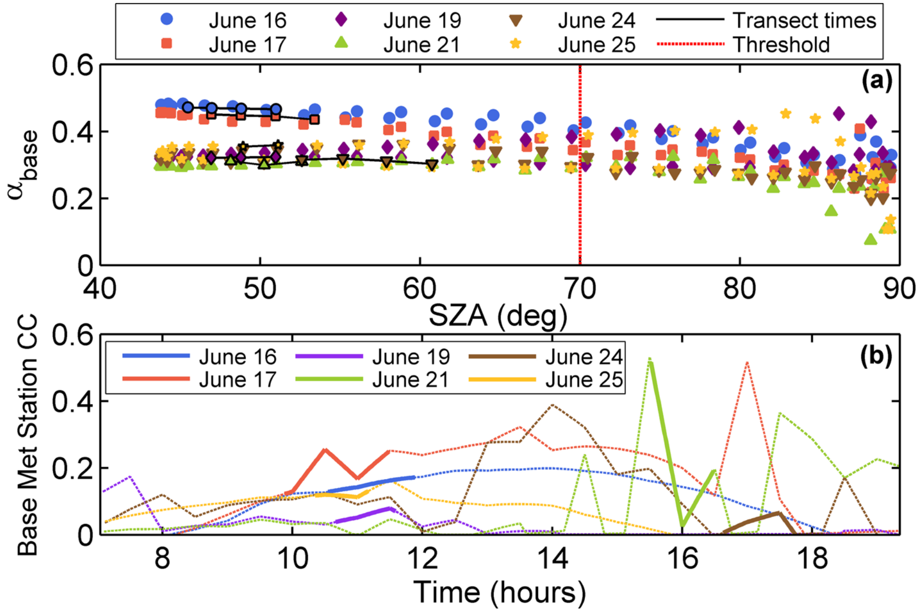

Figure 3. Half hourly broadband α_{base} **(a)** measurements as a function of SZA. Symbols and colors correspond to transect dates. Transect times correspond to the black line. A SZA threshold at 70° is represented by the red stipple line. **(b)** Relative CC determined at α_{base} as a function of time during transect dates. Symbols and colors correspond to transect dates. Transect times correspond to bold lines.

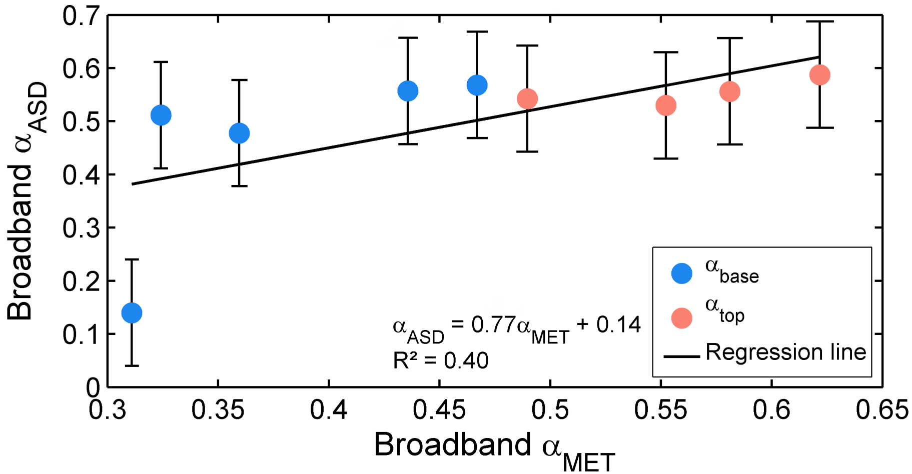

Figure 4. Broadband α_{base} (blue dots) and α_{top} (pink dots) vs. α_{ASD} and α_{MET} (i.e., both α_{base} and α_{top}) measurements fitted to a linear regression equation ($R^2 = 0.40$). The value of α_{ASD} error is unknown, but a conservative estimate of ±0.1 is shown.

TCD
8, 4737–4778, 2014

Bimodal albedo distributions in the ablation zone of the southwestern GrIS

S. E. Moustafa et al.

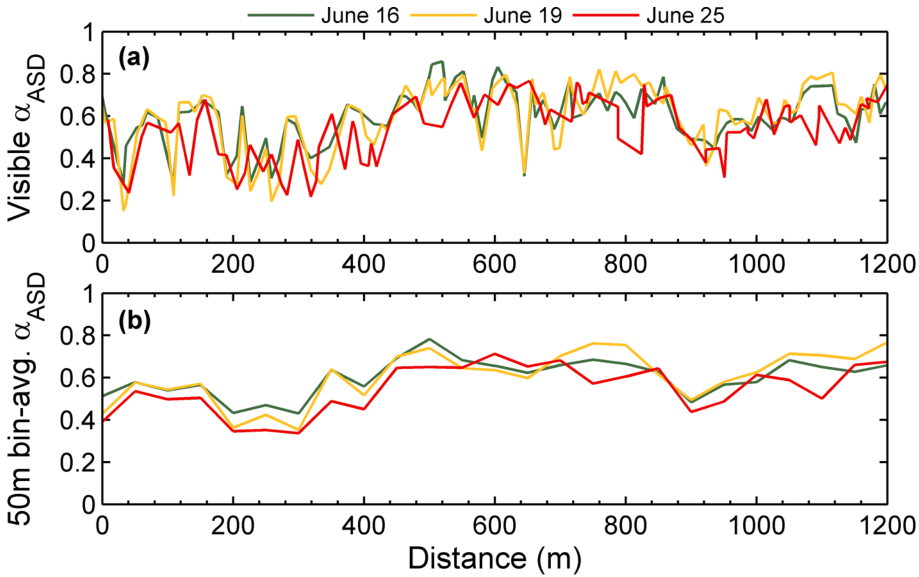

Figure 5. High-quality visible α_{ASD} observations on 16, 19 and 25 June **(a)**, and visible α_{ASD} averaged in 50 m bins **(b)** along the length of the transect starting near Site E (0 m) and ending near Site A (1200 m).

TCD
8, 4737–4778, 2014

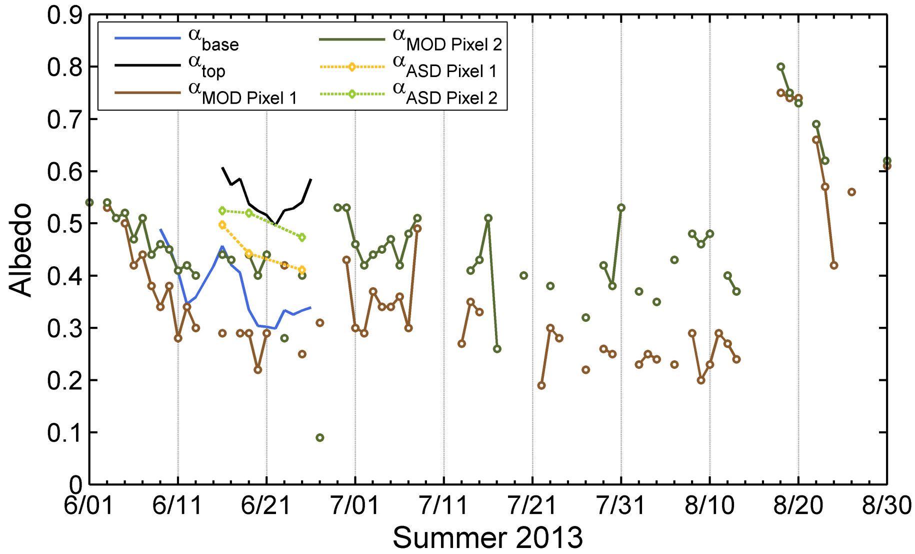

Figure 6. High-quality daily average broadband $\alpha_{ASD\ Pixel\ 1}$ and $\alpha_{ASD\ Pixel\ 2}$, α_{base} and α_{top} (for SZA < 70°), and $\alpha_{MOD\ Pixel\ 1}$ and $\alpha_{MOD\ Pixel\ 2}$ time series for the 2013 melt season. $\alpha_{ASD\ Pixel\ 1}$ and $\alpha_{ASD\ Pixel\ 2}$ pixel-averaged values correspond to high-quality ASD transect dates 16, 19 and 25 June.

TCD
8, 4737–4778, 2014

Bimodal albedo distributions in the ablation zone of the southwestern GrIS

S. E. Moustafa et al.

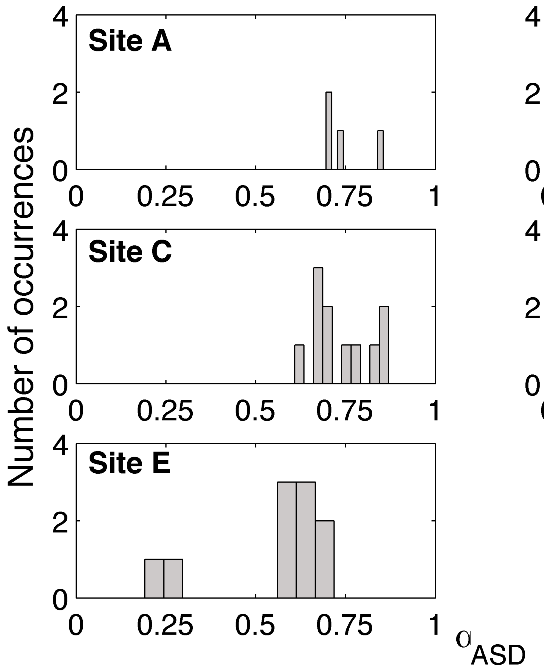

Figure 7. Distribution of visible α_{ASD} within 10 m radius of ablation stake sites.

TCD
8, 4737–4778, 2014

Bimodal albedo distributions in the ablation zone of the southwestern GrIS

S. E. Moustafa et al.

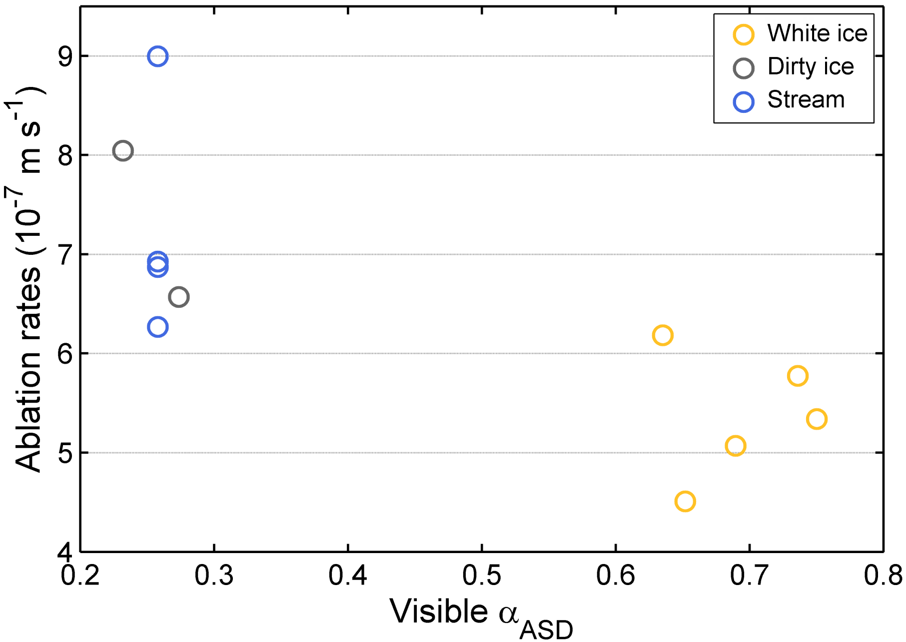

Figure 8. Observed ablation rates and visible α_{ASD} for different ice surface types.

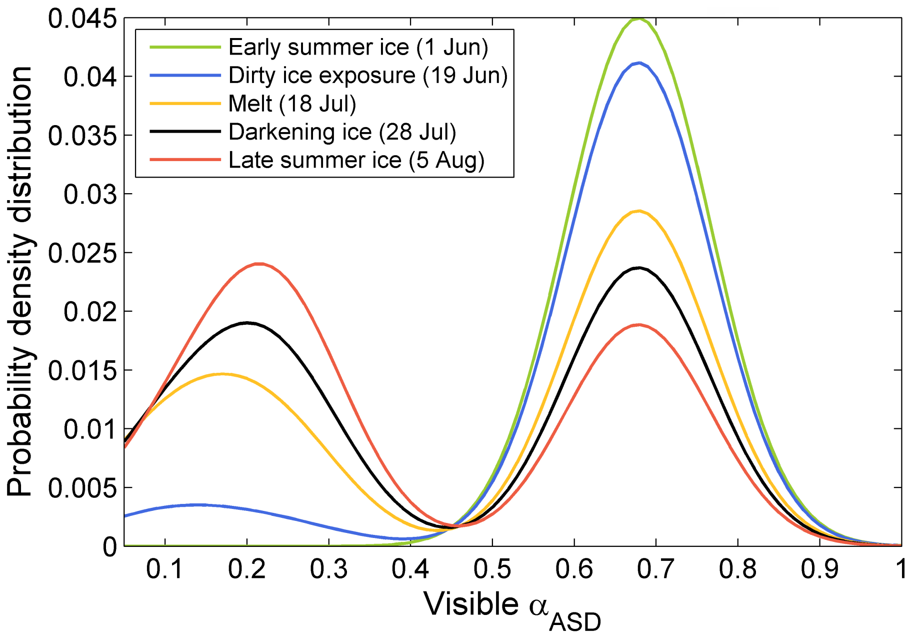

Figure 9. Computed albedo distribution simulated across the melt season based on observed visible α_{ASD} values for dominant surface types, weighted by their relative surface area coverage. Each surface type is assumed to follow a normal distribution. Computed albedo distributions represent the sum of each surface type's probability distribution function.

TCD
8, 4737–4778, 2014

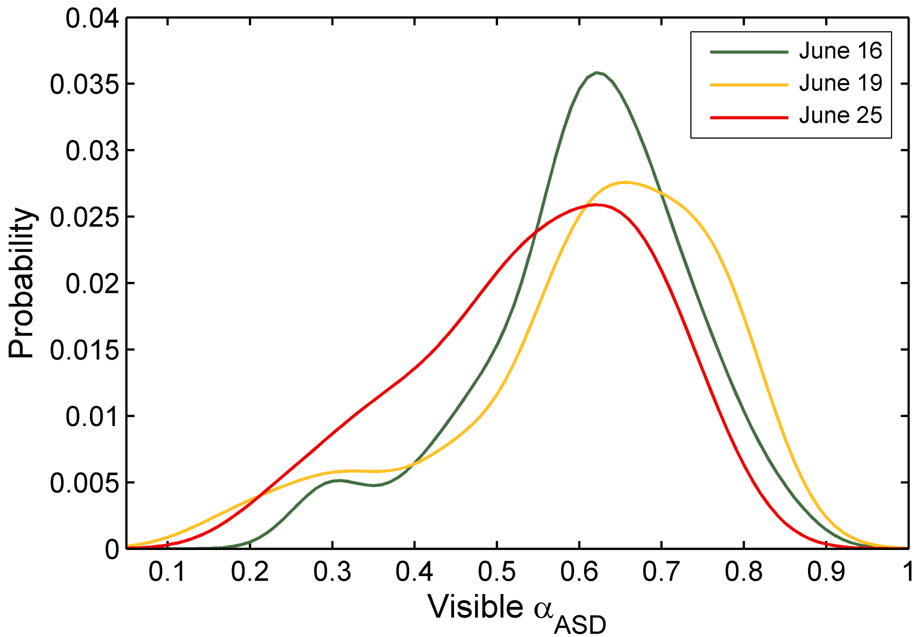

Figure 10. Observed distributions of high-quality visible α_{ASD} transects on 16, 19, and 25 June.

TCD
8, 4737–4778, 2014

Bimodal albedo distributions in the ablation zone of the southwestern GrIS

S. E. Moustafa et al.

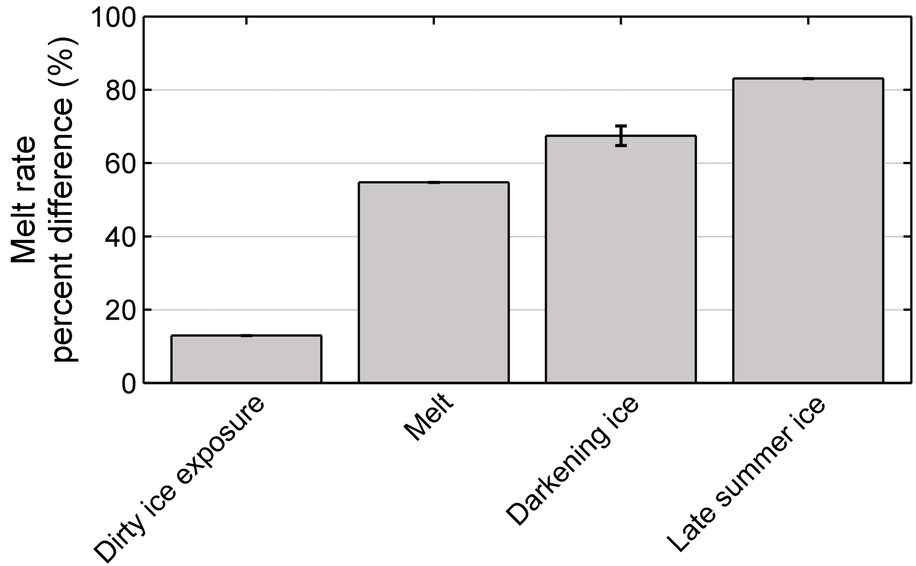

Figure 11. Percent difference in melt rate estimates for different albedo probability density functions and averaged incoming solar radiation conditions at Base Met Station from 16, 19, and 25 June.

TCD
8, 4737–4778, 2014

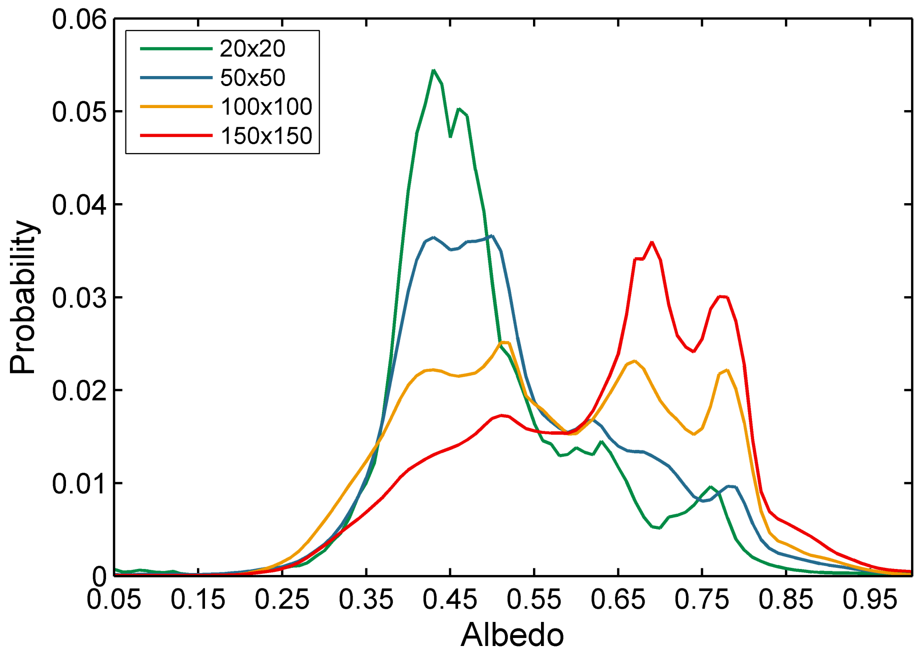

Figure 12. MOD10A1 2013 seasonal average albedo probability density distributions at four spatial scales. A bimodal albedo distribution is evident at the 100 × 100 (46.3 km^2) spatial extent.

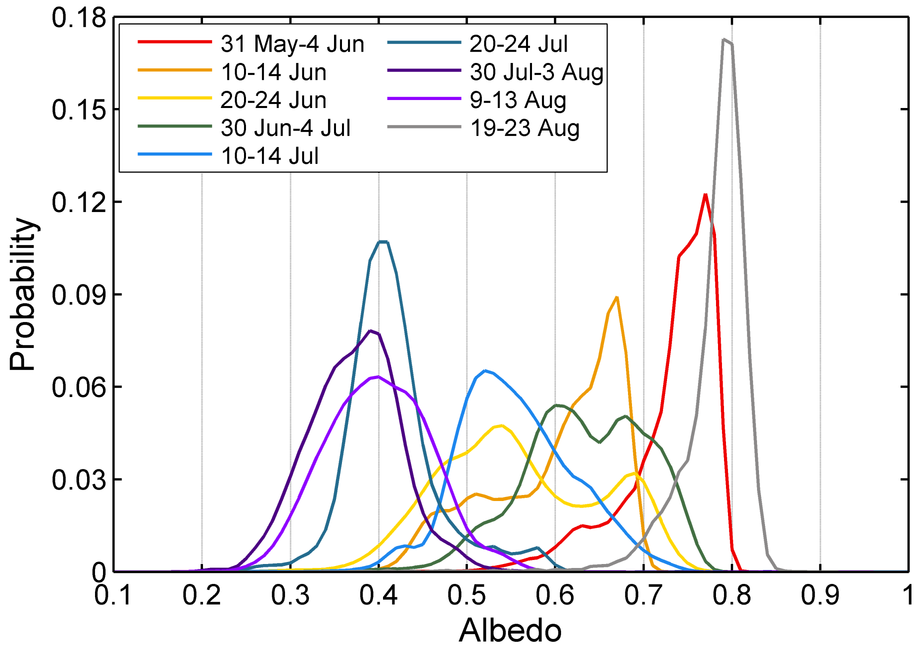

Figure 13. 100 × 100 pixel scale pentad averages over the 2013 melt season. Every other pentad average line is plotted.

TCD
8, 4737–4778, 2014

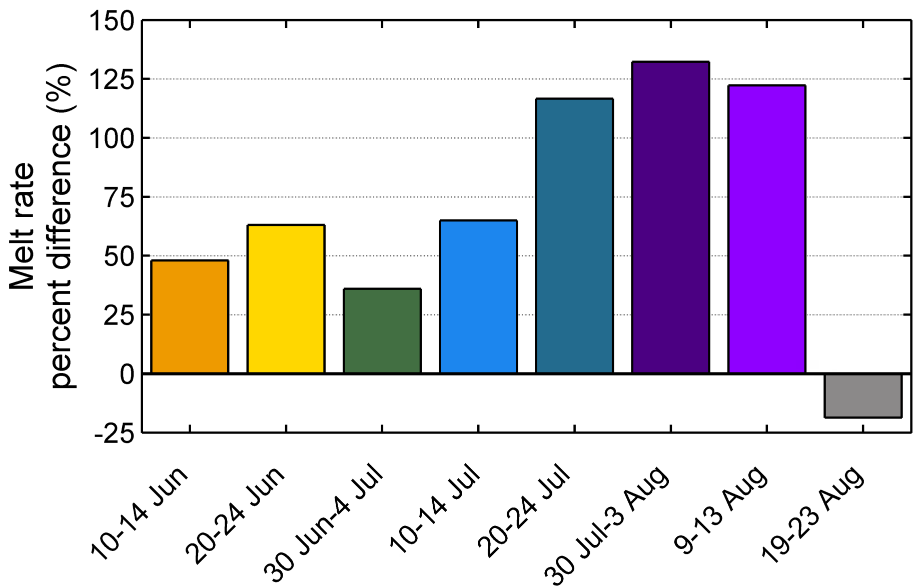

Figure 14. Percent difference in melt rate estimates for 100 × 100 pentad averages for the 2013 melt season, relative to 31 May to 4 June pentad average distribution.

TCD
8, 4737–4778, 2014